JOURNAL OF GUIDANCE, CONTROL, AND DYNAMICS
Vol. 30, No. 2, March–April 2007

Primer Vector Theory Applied to Global Low-Thrust Trade Studies

Ryan P. Russell*
Jet Propulsion Laboratory, California Institute of Technology, Pasadena, California 91109

DOI: 10.2514/1.22984

The low-thrust spacecraft trajectory problem can be reduced to only a few parameters using calculus of variations and the well-known primer vector theory. This low dimensionality combined with the extraordinary speed of modern computers allows for rapid exploration of the parameter space and invites opportunities for global optimization. Accordingly, a general low-thrust trade analysis tool is developed based on a global search for local indirect method solutions. An efficient propagator is implemented with an implicit "bang-bang" thrusting structure that accommodates an a priori unknown number of switching times. An extension to the standard adjoint control transformation is introduced that provides additional physical insight and control over the anticipated evolution of the thrust profile. The uniformly random search enjoys a perfect linear speedup for parallel implementation. The method is applied specifically on multirevolution transfers in the Jupiter–Europa and Earth–moon restricted three body problems. In both cases, thousands of solutions are found in a single parallel run. The result is a global front of Pareto optimal solutions across the competing objectives of flight time and final mass.

Introduction

THE extraordinary speeds of modern computers provide new opportunities for applications of established concepts such as the primer vector theory [1–3] and the low-thrust spacecraft problem. Traditionally, indirect optimization methods enjoy fewer dimensions in the search space, but suffer accordingly with extreme sensitivities to the search parameters. The methods typically have excellent convergence properties when the initial guess is near a solution, but the inherent sensitivities imply a small radius of convergence. In general, a linear or even quadratic Taylor series approximation to the constraints and objectives is only valid for a very small region centered about an initial guess. Additionally, indirect methods are difficult to generalize for higher fidelity models and atypical constraints. As a result, in this age of modern computing, indirect methods have lost much of their appeal when compared to the higher dimensioned, direct methods that are generally more stable and easier to modify for general problems and constraints. In this paper, the indirect method is revisited in a modern context. More specifically, the low-thrust spacecraft problem is reduced to a few dimensions using the well-known primer vector theory, and the low dimensionality combined with the fast modern computers allows for a broad perspective of optimal trajectories in a multiobjective landscape.

Before the advent of the modern computer, the only optimal control problems that could realistically be solved were those with analytic solutions. The low-thrust spacecraft problem is generally not amenable to analytic solutions and therefore cannot be solved in any practical sense without numerical methods. The anticipation and introduction of the computer in the 1950s and 60s then paved the way for Lawden [1], Marec [2], Jezewski [3], Melbourne and Sauer [4,5], and others to apply the well-established principles of calculus of variations [6,7] specifically to the low-thrust spacecraft trajectory problem. Primer vector theory was born and the young astrodynamic community enjoyed a quantum leap in terms of its ability to find optimal spacecraft trajectories. Of course, in addition to the finite-thrust application, primer vector theory is also useful for impulsive trajectory optimization. See, for example, [8–13]. However, in this paper we limit our discussion and application to low-thrust, constant specific impulse (I_{sp}) trajectories. For a sampling of other recent calculus of variations applications to low-thrust trajectory design, see [14–20].

When primer vector theory was first introduced, even with a good initial guess, a single solution required nontrivial computational times. Direct approaches with the huge dimensions that are common today were not realistic and as a result, the indirect methods received more attention primarily because they were feasible at the time. As the decades progressed and Moore's law [21] came to fruition, the higher dimensioned problems became more and more feasible, and scores of techniques were introduced to solve (with unprecedented success) the optimal control problem and the general nonlinear programming problem. Representative large-dimensioned methods include collocation or pseudospectral techniques [22–24], dynamic programming [25], static dynamic control [26], and sequential quadratic programming [27].

Although the higher dimensioned problems receive the most obvious benefits from computational speedups (because previously unapproachable problems are now readily solvable), the benefits bestowed on the lower dimensioned problems have received much less attention. For optimization or root-solving problems, it is often possible to perform exhaustive searches over the full range of the unknowns when the dimensions are sufficiently small and the objective or constraint function is sufficiently easy to calculate [28]. Even in cases when exhaustive searches are not feasible, a variety of techniques can be employed to rapidly sample and navigate global regions of search space. Thus, the problems of few dimensions are equally poised to benefit from the impressive speeds of modern computers.

In this paper, an efficient low-thrust trade analysis tool is described in a general context and implemented for practical examples dealing with multirevolution transfers in the Jupiter–Europa and Earth–moon restricted three body problems (RTBPs). The solution method is outlined including a modified adjoint control transformation, an implicit "bang-bang" thrusting structure, analytic derivatives for a local targeting search, and a uniformly random approach to a global search for mass optimal solutions across a wide range of flight times.

Presented as Paper AAS 06-156 at the AAS/AIAA Space Flight Mechanics Meeting, Tampa, Florida,, 22–26 January 2006; received 4 February 2006; revision received 29 May 2006; accepted for publication 28 June 2006.

*Technical Staff Member, Jet Propulsion Laboratory, 4800 Oak Grove Drive, M/S 301-140L; Ryan.Russell@jpl.nasa.gov. Member AIAA. Member AAS.

The tool is described and tested on two specific examples. The first is a target phase-free transfer between two distant retrograde orbits (DROs) at Europa, while the second is a target phase-free transfer from a distant near-circular orbit at Earth to a DRO at the moon. The method and equations are developed in a general three-dimensional form. However, the two examples are constrained to the planar case for simplicity.

Because the search space is uniformly populated with a random number generator, the speed improvements are linear for parallel implementation across independent processors. Tens of thousands of solutions are documented leading to well-defined Pareto fronts of nondominated solutions in the competing objectives of flight time and Δv. Resulting transfers generally have on the order of 5–15 revolutions and 0–50 implicitly solved bang-bang switching times. In the extreme cases, we find solutions approaching 100 revolutions and 100 switching times. We note that [29,30] complement this paper by solving similar multiobjective multirevolution trajectory problems. These references do not implement a gradient-based local search, but instead navigate the global space with evolutionary techniques that are driven by the propagator described in this paper.

Primer Vector Control Law

For a minimum fuel time-fixed orbit transfer, the optimal control problem is to minimize the performance index

$$J = -k(m_f) \tag{1}$$

subject to the dynamic, control, and terminal constraints, respectively:

$$\dot{\boldsymbol{X}} \equiv \begin{pmatrix} \dot{\boldsymbol{r}} \\ \dot{\boldsymbol{v}} \\ \dot{m} \end{pmatrix} = \boldsymbol{f}(\boldsymbol{X}, \boldsymbol{u}) \equiv \begin{pmatrix} \boldsymbol{v} \\ \boldsymbol{g}(\boldsymbol{r}) + \boldsymbol{h}(\boldsymbol{v}) + \boldsymbol{u}T/m \\ -T/c \end{pmatrix} \tag{2}$$

$$\boldsymbol{u}^{\mathsf{T}}\boldsymbol{u} = 1, \qquad T = T_{\max}\sin^2\sigma \tag{3}$$

$$\begin{aligned} &\boldsymbol{r}_f = \boldsymbol{r}^*(\tau_f), \qquad \boldsymbol{r}_0 = \boldsymbol{r}^*(\tau_0), \qquad \boldsymbol{v}_f = \boldsymbol{v}^*(\tau_f), \\ &\boldsymbol{v}_0 = \boldsymbol{v}^*(\tau_0), \qquad m_0 = m_0^*, \qquad t_f = t_f^*, \qquad t_0 = t_0^* \end{aligned} \tag{4}$$

where k is a constant positive multiplier, $\boldsymbol{g}$ and $\boldsymbol{h}$ are respectively functions of position and velocity only, $\boldsymbol{u}$ is the thrust direction, T is the thrust magnitude, σ is a slack control variable that enforces inequality bounds on T, τ is a timelike variable that uniquely parameterizes the initial and target orbits, $c = g_0 I_{\text{sp}}$ is the exhaust velocity, g_0 is the standard acceleration of gravity at the surface of the Earth, I_{sp} is the thruster specific impulse, and the superscript $*$ indicates a user specified value. Each constraint is accommodated by augmenting the performance index with a Lagrange multiplier,

$$\begin{aligned} J' = &-k(m_f) + \boldsymbol{\upsilon}_1^{\mathsf{T}}[\boldsymbol{r}_f - \boldsymbol{r}^*(\tau_f)] + \boldsymbol{\upsilon}_2^{\mathsf{T}}[\boldsymbol{r}_0 - \boldsymbol{r}^*(\tau_0)] \\ &+ \boldsymbol{\upsilon}_3^{\mathsf{T}}[\boldsymbol{v}_f - \boldsymbol{v}^*(\tau_f)] + \boldsymbol{\upsilon}_4^{\mathsf{T}}[\boldsymbol{v}_0 - \boldsymbol{v}^*(\tau_0)] + \upsilon_5(m_0 - m_0^*) \\ &+ \upsilon_6(t_f - t_f^*) + \upsilon_7(t_0 - t_0^*) + \int \{\boldsymbol{\lambda}^{\mathsf{T}}(\boldsymbol{f} - \dot{\boldsymbol{X}}) + \eta_1(\boldsymbol{u}^{\mathsf{T}}\boldsymbol{u} - 1) \\ &+ \eta_2(T - T_{\max}\sin^2\sigma)\}\,\mathrm{d}t \end{aligned} \tag{5}$$

The constraints that apply over the whole trajectory are included inside the integral while the boundary constraints remain on the outside. The multipliers inside the integral are functions of time while those on the outside are constants. If all of the constraints are met, J' is identical to and has the same extremals as the original performance index J. We introduce the Hamiltonian H, by rewriting Eq. (5) and expanding the definitions for $\boldsymbol{f}$ and $\boldsymbol{\lambda}$,

$$J' = \Theta + \int (\hat{H} - \boldsymbol{\lambda}^{\mathsf{T}}\dot{\boldsymbol{X}})\,\mathrm{d}t \tag{6}$$

where

$$\begin{aligned} \hat{H} &= H + \eta_1(\boldsymbol{u}^{\mathsf{T}}\boldsymbol{u} - 1) + \eta_2(T - T_{\max}\sin^2\sigma) \\ H &= \boldsymbol{\lambda}_r^{\mathsf{T}}\boldsymbol{v} + \boldsymbol{\lambda}_v^{\mathsf{T}}(\boldsymbol{g} + \boldsymbol{h} + \boldsymbol{u}T/m) - \lambda_m T/c \\ \Theta &= -km_f + \boldsymbol{\upsilon}_1^{\mathsf{T}}[\boldsymbol{r}_f - \boldsymbol{r}^*(\tau_f)] + \boldsymbol{\upsilon}_2^{\mathsf{T}}[\boldsymbol{r}_0 - \boldsymbol{r}^*(\tau_0)] \\ &\quad + \boldsymbol{\upsilon}_3^{\mathsf{T}}[\boldsymbol{v}_f - \boldsymbol{v}^*(\tau_f)] + \boldsymbol{\upsilon}_4^{\mathsf{T}}[\boldsymbol{v}_0 - \boldsymbol{v}^*(\tau_0)] + \upsilon_5(m_0 - m_0^*) \\ &\quad + \upsilon_6(t_f - t_f^*) + \upsilon_7(t_0 - t_0^*) \end{aligned} \tag{7}$$

The necessary conditions for a minimum of J' are derived by setting the differential, $\mathrm{d}J'$ equal to zero, thus leading to the well-known Euler–Lagrange equations and associated boundary conditions known as transversality conditions. For a detailed derivation see [7,31]. The Euler–Lagrange equations (8–11) provide equations of motion for $\boldsymbol{\lambda}$, the Lagrange multipliers associated with the state, and provide conditions for choosing the control parameters, T, $\boldsymbol{u}$, and σ.

$$\dot{\boldsymbol{\lambda}} = -\left(\frac{\partial \hat{H}}{\partial \boldsymbol{X}}\right)^{\mathsf{T}} \tag{8}$$

$$\boldsymbol{0} = \left(\frac{\partial \hat{H}}{\partial \boldsymbol{u}}\right)^{\mathsf{T}} = \boldsymbol{\lambda}_v T/m + 2\eta_1 \boldsymbol{u} \tag{9}$$

$$0 = \frac{\partial \hat{H}}{\partial T} = \boldsymbol{\lambda}_v^{\mathsf{T}}\boldsymbol{u}/m - \lambda_m/c + \eta_2 \tag{10}$$

$$0 = \frac{\partial \hat{H}}{\partial \sigma} = -2\eta_2 T_{\max}\sin\sigma\cos\sigma \tag{11}$$

Equation (9) indicates that either $\boldsymbol{\lambda}_v$ is parallel to $\boldsymbol{u}$ or T and η_1 are zero or $\boldsymbol{\lambda}_v$ and η_1 are zero. Because the latter two are not true in general, we conclude that $\boldsymbol{u} = \boldsymbol{\lambda}_v/\lambda_v$ or $\boldsymbol{u} = -\boldsymbol{\lambda}_v/\lambda_v$. To choose the direction, we rely on the Weierstrass condition [7] or Pontryagin's maximum principle. Both reveal that a necessary condition for a minimum requires that the admissible controls are chosen such that the Hamiltonian H is minimized at all points along the path. From Eq. (7), H is clearly minimized when $\boldsymbol{u} = -\boldsymbol{\lambda}_v/\lambda_v$. Eliminating $\boldsymbol{u}$ from H,

$$H = \boldsymbol{\lambda}_r^{\mathsf{T}}\boldsymbol{v} + \boldsymbol{\lambda}_v^{\mathsf{T}}(\boldsymbol{g} + \boldsymbol{h}) - (T/m)S \tag{12}$$

where a switching function is defined,

$$S = (\lambda_v + \lambda_m m/c) \tag{13}$$

Again applying the minimum principle or the Weierstrass condition with respect to the other control T, we find that H is minimized if $T = T_{\max}$ when $S > 0$ and $T = 0$ when $S < 0$. When $S = 0$, then $0 \le T \le T_{\max}$. This logic is consistent with Eqs. (10) and (11), where Eq. (11) requires that either η_2, $\cos\sigma$, or $\sin\sigma$ is zero. Looking at the thrust constraint in Eq. (7), if $\cos\sigma = 0$, then $T = T_{\max}$. If $\sin\sigma = 0$, then $T = 0$. Lastly, if $\eta_2 = 0$, then σ is undetermined and thus $0 \le T \le T_{\max}$. Furthermore, combining Eqs. (10) and (13) yields $S = \eta_2 m$. Therefore, if $\eta_2 = 0$, then T is undetermined because $S = 0$.

Lawden's well-known primer vector control law is summarized in Eq. (14), where $\boldsymbol{p}$ is defined as the primer vector [1]:

$$\boldsymbol{u} = -\frac{\boldsymbol{\lambda}_v}{\lambda_v} \equiv \frac{\boldsymbol{p}}{p}, \qquad T = \begin{cases} 0 & \text{if } S < 0 \\ T_{\max} & \text{if } S > 0 \\ 0 \le T \le T_{\max} & \text{if } S = 0 \end{cases} \tag{14}$$

Applying Eqs. (8) and (12) the equations of motion for the state Lagrange multipliers, also known as the costates, become

$$\dot{\boldsymbol{\lambda}}_r = -\boldsymbol{G}^\mathsf{T}\boldsymbol{\lambda}_v, \qquad \dot{\boldsymbol{\lambda}}_v = -\boldsymbol{\lambda}_r - \boldsymbol{H}^\mathsf{T}\boldsymbol{\lambda}_v, \qquad \dot{\lambda}_m = -\lambda_v T/m^2$$
$$\boldsymbol{G} = \partial \boldsymbol{g}/\partial \boldsymbol{r}, \qquad \boldsymbol{H} = \partial \boldsymbol{h}/\partial \boldsymbol{v} \tag{15}$$

Note that if H does not include an explicit time dependence, it can be shown to be an integral of motion everywhere along the trajectory as long as Eqs. (8–11) are satisfied. This constant of motion holds across all switching times and is useful as an integration accuracy check.

In the case where $\boldsymbol{G} = \boldsymbol{G}^\mathsf{T}$ and $\boldsymbol{H} = -\boldsymbol{H}^\mathsf{T}$, it is well known and can be readily shown [13,32] that the primer vector $\boldsymbol{p}$ obeys the same differential equations as the variational equations that arise from linearizing the equations of motion for position and velocity in Eq. (2) while assuming a fixed thrust profile. The second order forms are

$$\delta\ddot{\boldsymbol{r}} = \boldsymbol{G}\delta\boldsymbol{r} + \boldsymbol{H}\delta\boldsymbol{v} \qquad \ddot{\boldsymbol{p}} = \boldsymbol{G}\boldsymbol{p} + \boldsymbol{H}\ddot{\boldsymbol{p}} \tag{16}$$

Therefore, as Marec discusses on p. 59 of [2], the physical interpretation of the primer vector is as follows: "The optimal thrust acceleration (paying no attention to boundary conditions)... points towards a neighboring moving point being subjected to the same gravitational field and same thrust acceleration as the moving (spacecraft)." Thus, it is possible to implement the primer vector control law without using the costate or variational equations entirely. The primer thrust direction can be approximated as the connecting line between two spacecraft propagated with neighboring initial conditions using the state equations only. This physical notion of the primer vector helps to explain its cyclic nature, and how it is possible, with only a handful of initial control variables, to navigate a spacecraft through potentially hundreds of revolutions and switching times in a strikingly well-organized fashion.

Note that the more complicated formal second order sufficient conditions for a minimum are not considered in this study. Alternatively, by seeking an abundance of solutions that satisfy the necessary conditions, it is anticipated that the best of these solutions represent minima and therefore implicitly and informally satisfy the sufficient conditions. For recent applications of primer vector theory that specifically consider the second order conditions, see [33].

Two Point Boundary Value Problem (TPBVP)

The natural boundary conditions are also first-order necessary conditions for optimality and are derived in the same manner as the Euler–Lagrange equations. For the time-fixed orbit transfer problem, in order for J' from Eq. (6) to be stationary, it can be shown that

$$\begin{aligned}
&\partial\Theta/\partial t_f = -H_f \Rightarrow H_f = -\upsilon_6 \qquad \partial\Theta/\partial t_0 = H_0 \Rightarrow H_0 = \upsilon_7\\
&\partial\Theta/\partial \boldsymbol{X}_f = \boldsymbol{\lambda}_f^\mathsf{T} \Rightarrow (\boldsymbol{\lambda}_{rf}^\mathsf{T}\ \boldsymbol{\lambda}_{vf}^\mathsf{T}\ \lambda_{mf}) = (\boldsymbol{\upsilon}_1^\mathsf{T}\ \boldsymbol{\upsilon}_3^\mathsf{T}\ -k)\\
&\partial\Theta/\partial \boldsymbol{X}_0 = -\boldsymbol{\lambda}_0^\mathsf{T} \Rightarrow (\boldsymbol{\lambda}_{r0}^\mathsf{T}\ \boldsymbol{\lambda}_{v0}^\mathsf{T}\ \lambda_{m0}) = (-\boldsymbol{\upsilon}_2^\mathsf{T}\ -\boldsymbol{\upsilon}_4^\mathsf{T}\ -\upsilon_5)\\
&\partial\Theta/\partial\tau_f = 0 \Rightarrow \boldsymbol{\lambda}_{rf}^\mathsf{T}\boldsymbol{v}_f + \boldsymbol{\lambda}_{vf}^\mathsf{T}(\boldsymbol{g}_f + \boldsymbol{h}_f) = 0\\
&\partial\Theta/\partial\tau_0 = 0 \Rightarrow \boldsymbol{\lambda}_{r0}^\mathsf{T}\mathbf{v}_0 + \boldsymbol{\lambda}_{v0}^\mathsf{T}(\boldsymbol{g}_0 + \boldsymbol{h}_0) = 0
\end{aligned} \tag{17}$$

The last two equations are the only ones that do not introduce additional unknown parameters. Thus, for the specific case of the time-fixed orbit transfer problem, the TPBVP is reduced to eight dimensions. The unknown and constraint vectors are given in Eq. (18). To reduce the number of unknowns, we set $\lambda_{m0} = -1$. The final condition $\lambda_m = -k$ is automatically because λ_m monotonically decreases.

$$\boldsymbol{U}_{8\times1} = \begin{pmatrix} \boldsymbol{\lambda}_{r0} \\ \boldsymbol{\lambda}_{v0} \\ \tau_f \\ \tau_0 \end{pmatrix} \qquad \boldsymbol{C}_{8\times1} = \begin{pmatrix} \boldsymbol{r}_f - \boldsymbol{r}^*(\tau_f) \\ \boldsymbol{v}_f - \boldsymbol{v}^*(\tau_f) \\ \boldsymbol{\lambda}_{rf}^\mathsf{T}\boldsymbol{v}_f + \boldsymbol{\lambda}_{vf}^\mathsf{T}(\boldsymbol{g}_f + \boldsymbol{h}_f) = 0 \\ \boldsymbol{\lambda}_{r0}^\mathsf{T}\boldsymbol{v}_0 + \boldsymbol{\lambda}_{v0}^\mathsf{T}(\boldsymbol{g}_0 + \boldsymbol{h}_0) = 0 \end{pmatrix} \tag{18}$$

If the initial or final time is changed to a free parameter, the associated constraint in Eq. (4) is removed, and from Eq. (17), the additional transversality condition becomes $H_0 = 0$ or $H_f = 0$, respectively. Likewise, if the initial or final τ is changed to a fixed parameter, then the associated unknown and constraint are removed accordingly from Eq. (18).

Restricted Three Body Problem (RTBP)

The primer vector control law and TPBVP as presented are applicable for any dynamic system that can be expressed in the form of Eq. (2). In this paper, both numerical examples are based on the RTBP. The expressions for $\boldsymbol{g}$ and $\boldsymbol{h}$ specific to the RTBP are given in Eq. (19).

$$\boldsymbol{g}(\boldsymbol{r}) = \begin{bmatrix} (r_1 + 1 - \mu) + \kappa(r_1 + 1) + \mu/r^3 \\ r_2(1 + \kappa) \\ \kappa r_3 \end{bmatrix}$$
$$\boldsymbol{h}(\boldsymbol{v}) = \begin{bmatrix} 2v_2 \\ -2v_1 \\ 0 \end{bmatrix} \qquad \kappa = -(1-\mu)/\rho^3 - \mu/r^3 \tag{19}$$
$$\mu = Gm_r/(Gm_r + Gm_\rho) \qquad \rho = \sqrt{(r_1+1)^2 + r_2^2 + r_3^2}$$
$$r = \sqrt{r_1^2 + r_2^2 + r_3^2}$$

The RTBP equations of motion are presented in the standard rotating frame that assumes the two celestial bodies orbit their common center of mass with a constant separation of 1 length unit (LU) and an orbital rate of 1 rad per time unit (TU). The coordinate frame is centered at the smaller mass, the r_1 axis points away from the larger mass, and the r_3 axis points toward the system angular momentum. The spacecraft distances to the large and small masses are denoted as ρ and r, respectively. Similarly, the gravitational parameters are Gm_ρ and Gm_r. The RTBP is a Hamiltonian system and admits the integral of motion C, known as the Jacobi constant.

$$C = (r_1 + 1 - \mu)^2 + r_2^2 + 2(1-\mu)/\rho + 2\mu/r - v_1^2 - v_2^2 - v_3^2 \tag{20}$$

The gradients, $\boldsymbol{G}(\boldsymbol{r})$ and $\boldsymbol{H}(\boldsymbol{v})$, necessary to propagate the costate equations from Eq. (15) are given in Eq. (21).

$$\begin{aligned}
G_{1,1} &= (1-\mu)[2(r_1+1)^2 - r_2^2 - r_3^2]/\rho^5 + \mu(2r_1^2 - r_2^2 - r_3^2)/r^5 \\
&\quad + 1\\
G_{2,2} &= (1-\mu)[2r_2^2 - (r_1+1)^2 - r_3^2]/\rho^5 + \mu(2r_2^2 - r_1^2 - r_3^2)/r^5 \\
&\quad + 1\\
G_{3,3} &= (1-\mu)[2r_3^2 - (r_1+1)^2 - r_2^2]/\rho^5 + \mu(2r_3^2 - r_1^2 - r_2^2)/r^5 \\
&\quad + 1\\
G_{1,2} &= G_{2,1} = 3(1-\mu)(r_1+1)r_2/\rho^5 + 3\mu r_1 r_2/r^5\\
G_{1,3} &= G_{3,1} = 3(1-\mu)(r_1+1)r_3/\rho^5 + 3\mu r_1 r_3/r^5\\
G_{2,3} &= G_{3,2} = 3(1-\mu)r_2 r_3/\rho^5 + 3\mu r_2 r_3/r^5\\
\boldsymbol{H} &= \begin{bmatrix} 0 & 2 & 0 \\ -2 & 0 & 0 \\ 0 & 0 & 0 \end{bmatrix}
\end{aligned} \tag{21}$$

Solution Method

Next, highlights of the solution method are discussed and the global low-thrust trade study algorithm is presented.

Adjoint Control Transformation

Estimating the initial costate values for the TPBVP can be difficult and nonintuitive. One approach is to solve a simpler problem with analytic results to approximate the optimal initial costates in the full problem [34]. For broader applications, Dixon and Biggs [35] first

introduced the idea to estimate physical control variables and their derivatives instead of the initial costates in order to reduce problem sensitivity and provide more of a physical significance. For example applications of this principle, see [14,15,36]. In particular, [14,15] provide the mapping $\mathcal{M}_1$: $(\alpha, \dot{\alpha}, \beta, \dot{\beta}, \lambda_{v0}, \dot{\lambda}_{v0}) \rightarrow (\boldsymbol{\lambda}_{r0}, \boldsymbol{\lambda}_{v0})$, where α and β are the in- and out-of-plane orientation angles, respectively, that represent the direction of the initial thrust $\boldsymbol{u}'$, in a spacecraft velocity centered frame. The mapping is summarized in Eq. (22) where the hat on a vector indicates it is of unit length. Note, this mapping includes the angular momentum vector and thus can flip directions frequently unless the spacecraft is in a simple circulating orbit. To alleviate this problem, alternative definitions of the in- and out-of-plane directions can be made. For our purposes, however, the flipping has no consequence because we only use the transformation at the initial time.

$$\boldsymbol{u}' = [\cos(\alpha)\cos(\beta)\ \ \sin(\alpha)\cos(\beta)\ \ \sin(\beta)]^{\mathsf{T}}$$

$$\dot{\boldsymbol{u}}' = \begin{bmatrix} -\sin(\alpha)\dot{\alpha}\cos(\beta) - \cos(\alpha)\sin(\beta)\dot{\beta} \\ \cos(\alpha)\dot{\alpha}\cos(\beta) - \sin(\alpha)\sin(\beta)\dot{\beta} \\ \cos(\beta)\dot{\beta} \end{bmatrix}$$

$$\boldsymbol{\omega} = \boldsymbol{r} \times \boldsymbol{v}$$

$$\dot{\boldsymbol{\omega}} = \boldsymbol{r} \times \dot{\boldsymbol{v}}$$

$$\dot{\omega} = \boldsymbol{\omega} \cdot \dot{\boldsymbol{\omega}}/\omega$$

$$\dot{\hat{\boldsymbol{\omega}}} = \dot{\boldsymbol{\omega}}/\omega - \boldsymbol{\omega}\dot{\omega}/\omega^2$$

$$\dot{v} = \boldsymbol{v} \cdot \dot{\boldsymbol{v}}/v$$

$$\dot{\hat{\boldsymbol{v}}} = \dot{\boldsymbol{v}}/v - \boldsymbol{v}\dot{v}/v^2 \tag{22}$$

$$\boldsymbol{R} = [\hat{\boldsymbol{v}}|\hat{\boldsymbol{\omega}} \times \hat{\boldsymbol{v}}|\hat{\boldsymbol{\omega}}]$$

$$\dot{\boldsymbol{R}} = [\dot{\hat{\boldsymbol{v}}}|\dot{\hat{\boldsymbol{\omega}}} \times \hat{\boldsymbol{v}} + \hat{\boldsymbol{\omega}} \times \dot{\hat{\boldsymbol{v}}}|\dot{\hat{\boldsymbol{\omega}}}]$$

$$\boldsymbol{u} = \boldsymbol{R}\boldsymbol{u}'$$

$$\dot{\boldsymbol{u}} = \dot{\boldsymbol{R}}\boldsymbol{u}' + \boldsymbol{R}\dot{\boldsymbol{u}}'$$

$$\boldsymbol{\lambda}_v = -\lambda_v \boldsymbol{u}$$

$$\dot{\boldsymbol{\lambda}}_v = -\dot{\lambda}_v \boldsymbol{u} - \lambda_v \dot{\boldsymbol{u}}$$

$$\boldsymbol{\lambda}_r = \dot{\boldsymbol{\lambda}}_v - \boldsymbol{H}^{\mathsf{T}}\boldsymbol{\lambda}_v$$

To further provide influence over the initial evolution of the thrust vector, in Eq. (23) we introduce a second mapping $\mathcal{M}_2$: $(S_0, \dot{S}_0) \rightarrow (\lambda_{v0}, \dot{\lambda}_{v0})$. Estimating the initial value of the switching function and its derivative provides some control (albeit limited) over the thrusting structure of the resulting trajectory. This mapping is particularly useful for multirevolution transfers when multiple switching of the thrusting is expected or desired. For example, if an initial thrust is desired to be followed shortly by a switching time, then S can be initiated as a small positive value and its derivative set to a negative value. Similarly, if a continuous thrust is desired, then S can be initiated as a large positive value. By combining $\mathcal{M}_1$ and $\mathcal{M}_2$ we replace the unknown values of the initial position and velocity costates with the physically meaningful quantities α, β, S, and their time derivatives. As Senet, Ocampo, and Ranieri [14,35] argue, the sensitivity of the problem is also reduced because the spacecraft velocity frame is naturally more amenable to the problem. However, in this study the adjoint control transformation is only used for propagating the trajectories in the global search mode, whereas the local gradient-based targeting directly iterates on the costates. Therefore, the analytic derivatives are simplified and the computational efficiency is improved for the large-scale global search. Furthermore, the sensitivity improvement is more pronounced for initial phase-free or initial time-free transfers, whereas both of the examples in this paper are initial time and initial phase fixed.

$$\lambda_v = S - \lambda_m m/c, \qquad \dot{\lambda}_v = \dot{S} - \lambda_m \dot{m}/c - \dot{\lambda}_m m/c \tag{23}$$

Implicit Bang-Bang Thrusting

A fast propagator is designed to implement the primer vector control law including an implicit bang-bang control structure that is governed by the derived switching function S. A variable step Runge–Kutta 7(8) integrator is employed that interpolates to an exact stopping condition when the switching function changes sign; hence there are no discontinuities in the equations of motion for a particular leg. The propagator continues to cycle through a thrust leg followed by a coast leg until a maximum time is met or an alternate prescribed stopping condition is met. This two-state throttle structure of the control (on or off) is a tremendous advantage compared to other optimization techniques that predefine the switching structure of the trajectory and are forced to leave the switching times as free parameters. Additionally many other optimizers leave the thrust magnitude as a continuous variable free parameter because of gradient issues only to find that the converged solutions do indeed observe the bang-bang control feature. Although "singular arcs" exist where $S = 0$ for finite durations, they are rare for practical space trajectories. Accordingly, the described propagator will ignore the singular arc, only switching its current thrust state when S crosses the boundary of zero. The combined state and costate vector $\boldsymbol{Y}$, and their equations of motion are given in Eq. (24),

$$\dot{\boldsymbol{Y}} \equiv \begin{pmatrix} \dot{\boldsymbol{r}} \\ \dot{\boldsymbol{v}} \\ \dot{m} \\ \dot{\boldsymbol{\lambda}}_r \\ \dot{\boldsymbol{\lambda}}_v \\ \dot{\lambda}_m \end{pmatrix} = \boldsymbol{f}(\boldsymbol{Y}) \equiv \begin{pmatrix} \boldsymbol{v} \\ \boldsymbol{g}(\boldsymbol{r}) + \boldsymbol{h}(\boldsymbol{v}) - (\boldsymbol{\lambda}_v/\lambda_v)T/m \\ -T/c \\ -\boldsymbol{G}^{\mathsf{T}}\boldsymbol{\lambda}_v \\ -\boldsymbol{\lambda}_r - \boldsymbol{H}^{\mathsf{T}}\boldsymbol{\lambda}_v \\ -\lambda_v T/m^2 \end{pmatrix} \tag{24}$$

Analytic Derivatives

To target the constraints from Eq. (18) (or some variation) using a gradient-based nonlinear equation solver, the partial derivatives of the constraints with respect to the unknowns must be provided. The sensitivity issues common to indirect shooting methods clearly encourage the use of analytic derivatives rather than estimating them numerically [17,37]. Although the analytic derivatives lead to great improvements in accuracy and speed, the setup cost is nontrivial because they require rederivation each time the unknown or constraint vector changes. Nonetheless, for multiple-revolution

solutions that are highly sensitive to small initial perturbations, analytic derivatives are particularly important. Although not implemented here, automatic differentiation is an alternative approach for improved accuracy [38].

Analytic partial derivatives generally are calculated using some combination of the state transition matrix and the chain rule. The state transition matrix $\boldsymbol{\Phi}$ maps derivatives from one time to another on a given *continuous* trajectory because it is equivalent to the partial derivative of a final state with respect to an initial state. It is obtained by integrating the variational equations given in Eq. (26). For a detailed derivation, see, for example, [39]. Thus, for a problem with n states, the dimension of the propagation is increased by n^2. The Jacobian for the equations of motion in Eq. (24) is given in Eq. (27). Note, by setting $T = 0$, the Jacobian remains valid for a coast trajectory.

$$\boldsymbol{\Phi}(t, t_0) = \partial \boldsymbol{Y}(t)/\partial \boldsymbol{Y}(t_0) \tag{25}$$

$$\dot{\boldsymbol{\Phi}}(t, t_0) = (\partial \boldsymbol{f}/\partial \boldsymbol{Y})|_t \boldsymbol{\Phi}(t, t_0) \qquad \boldsymbol{\Phi}(t_0, t_0) = \boldsymbol{I}_{14\times 14} \tag{26}$$

$$(\partial \boldsymbol{f}/\partial \boldsymbol{Y}) = \begin{pmatrix} \boldsymbol{0} & \boldsymbol{I} & \boldsymbol{0} & \boldsymbol{0} & \boldsymbol{0} & \boldsymbol{0} \\ \boldsymbol{G} & \boldsymbol{H} & (\boldsymbol{\lambda}_v/\lambda_v)T/m^2 & \boldsymbol{0} & -(T/m)(\boldsymbol{I}/\lambda_v - \boldsymbol{\lambda}_v\boldsymbol{\lambda}_v^{\mathsf{T}}/\lambda_v^3) & \boldsymbol{0} \\ \boldsymbol{0} & \boldsymbol{0} & 0 & \boldsymbol{0} & \boldsymbol{0} & 0 \\ -\partial(\boldsymbol{G}^{\mathsf{T}}\boldsymbol{\lambda}_v)/\partial \boldsymbol{r} & \boldsymbol{0} & \boldsymbol{0} & \boldsymbol{0} & -\boldsymbol{G}^{\mathsf{T}} & \boldsymbol{0} \\ \boldsymbol{0} & -\partial(\boldsymbol{H}^{\mathsf{T}}\boldsymbol{\lambda}_v)/\partial \boldsymbol{v} & \boldsymbol{0} & -\boldsymbol{I} & -\boldsymbol{H}^{\mathsf{T}} & \boldsymbol{0} \\ \boldsymbol{0} & \boldsymbol{0} & 2\lambda_v T/m^3 & \boldsymbol{0} & -\boldsymbol{\lambda}_v^{\mathsf{T}} T/(\lambda_v m^2) & 0 \end{pmatrix} \tag{27}$$

As expressed, the state transition matrix maps perturbations across trajectory arcs with no discontinuities. However, the goal is to obtain the partial derivative of the final state with respect to the initial state and there may be several legs of thrust and coast with discontinuities across the boundaries (see Fig. 1). In Eq. (28), we string together a sequence of partial derivatives across N discontinuities using the chain rule, where each discontinuity is handled by introducing $\boldsymbol{\Psi}_n$, the partial derivative of the state at t_{n+} with respect to the state at t_{n-}.

$$\begin{aligned} &\partial \boldsymbol{Y}(t_f)/\partial \boldsymbol{Y}(t_0) \\ &\quad = \boldsymbol{\Phi}(t_f, t_{N+})\boldsymbol{\Psi}_N \boldsymbol{\Phi}(t_{N-}, t_{(N-1)+})\boldsymbol{\Psi}_{(N-1)} \cdots \boldsymbol{\Phi}(t_{2-}, t_{1+})\boldsymbol{\Psi}_1 \boldsymbol{\Phi}(t_{1-}, t_0) \end{aligned} \tag{28}$$

$$\begin{aligned} \boldsymbol{\Psi}_n \equiv \partial \boldsymbol{Y}(t_{n+})/\partial \boldsymbol{Y}(t_{n-}) = \{&\boldsymbol{I}_{14\times 14} + (\dot{\boldsymbol{Y}}|_{n+} \\ &- \dot{\boldsymbol{Y}}|_{n-})[\partial S/\partial \boldsymbol{Y})/\dot{S}]|_{n-}\} \end{aligned} \tag{29}$$

When a state Y_i at t_{n-} is perturbed (see Fig. 2), it causes the switching function to shift by $\delta S = \delta Y_i(\partial S/\partial Y_i)_{n-}$. Therefore, the switching time is perturbed by $\mathrm{d}t = -\delta S/\dot{S}_{n-} = -\delta Y_i(\partial S/\partial Y_i)_{n-}/\dot{S}_{n-}$. The change in the state Y_i at $t_n + \mathrm{d}t$ due only to the change in the switching time equals $(\dot{Y}_i|_{n-} - \dot{Y}_i|_{n+})\,\mathrm{d}t$. Thus the total change in the state at $t_n + \mathrm{d}t$ is given in Eq. (30), the scalar equivalent of Eq. (29). Note, if the discontinuity is not present across t_n, $\boldsymbol{\Psi}_n$ reduces to $\boldsymbol{I}$.

$$\delta Y_i|_{n+} = \delta Y_i|_{n-}[1 + (\dot{Y}_i|_{n+} - \dot{Y}_i|_{n-})(\partial S/\partial Y_i)_{n-}/\dot{S}_{n-}] \tag{30}$$

For implementation in a targeting routine, calculating the partial of a final time constraint (that is a function of the state) with respect to the initial state is simply the partial of the constraint function with respect to the state evaluated at the final time multiplied by the result from Eq. (28).

Pareto Optimality

In an optimization problem with competing objectives, such as time of flight and fuel expenditures, a Pareto front represents the best available solutions with regard to the trade space without the use of weighting functions. For an arbitrary set of solutions plotted in the flight time $-\Delta v$ plane, by definition, a Pareto optimal solution is one that finds no other that is better in both flight time and Δv. To determine if a particular solution is Pareto optimal, its flight time and Δv must be compared to all other solutions in the set. If any other solution is superior in both objectives, then the solution is not Pareto optimal. See Fig. 3 for an example Pareto front. Note that each Pareto solution sits on the upper right corner of a gray box that is empty of other solutions.

Multiobjective optimization via heuristic, gradient-based, evolutionary, and many other methods is a rapidly emerging field with potential for applications across many disciplines. For a general introduction, see [40]. In this study, the flight time $-\Delta v$ plane is populated with local Δv extremal solutions across a wide range of flight times. After the full set is assembled, each solution is examined against all other solutions to determine Pareto optimality.

With regard to a global trajectory search, the concept of Pareto optimality is powerful particularly because trajectories are sought with a priori unknown flight times. If a global search is conducted for

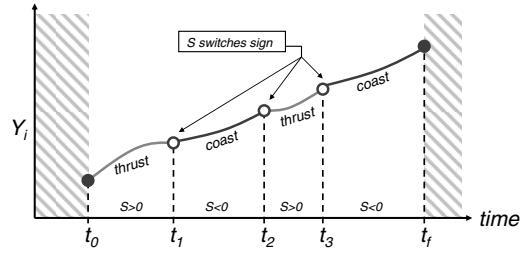

Fig. 1 Implicit "bang-bang" thrusting.

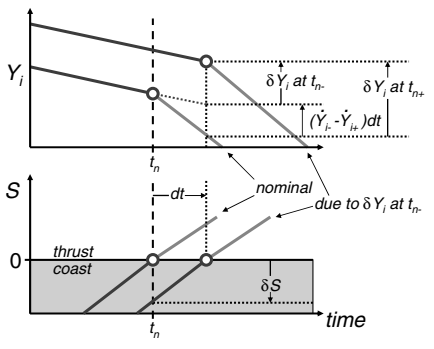

Fig. 2 Small perturbation effects on S and Y_i.

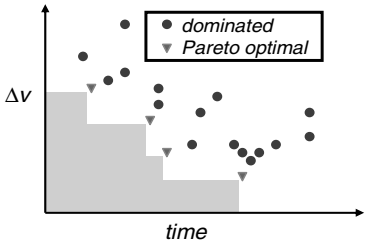

Fig. 3 Pareto front.

a fixed flight time trajectory, many of the search propagations are likely to ignorantly pass near solutions with smaller flight times. However, by checking the constraint functions at each time step along a trajectory, the scope of the search is only marginally widened, yet it brings the tremendous benefit of potentially finding a sweep of optimal or near-optimal solutions for a full range of flight times. Obtaining solutions for multiple times of flight via parametric studies and traditional methods can be tedious and difficult to tune. Furthermore, the parametric solutions inherently are related as a family of local solutions, whereas the Pareto optimal solutions may contain a variety of independent solution families and are thus more likely to represent global minima.

Local Search Strategy

The TPBVP described in Eq. (18) provides an equal number of unknowns and constraints for the general time-fixed phase-free orbit to orbit transfer. The necessary modifications are also given for time-free or phase-fixed orbit to orbit transfers.

In light of the multiobjective optimization strategy, we elect to ignore any transversality conditions (i.e., all necessary boundary conditions except the final position and velocity constraints) with the presumption that they are implicitly driven to zero in the direction of the Pareto front. Note, however, for the particular case of the many-revolution problem, satisfying the transversality conditions bears little significance because the phase and time of flight variations over just one orbit have only a marginal impact on the final objectives.

Because we attempt to drive the transversality conditions to zero implicitly with the Pareto optimization, generally there are fewer constraints than unknowns. The degrees of freedom relax the problem and allow for a larger pool of feasible trajectories. In fact, each trajectory that is feasible in the final position and velocity constraint actually meets the necessary optimality conditions for the subproblem that is time and phase fixed to the specific time and phase of the resulting solution.

For the local search, we use the "feasible point" mode of the gradient-based sequential quadratic programming software SNOPT [27] to target the final orbit constraints by adjusting the initial costates and any free times or phases. The first-order necessary conditions (ignoring the transversality conditions) are implicitly satisfied through the enforcement of the primer vector control law. The feasible point mode of SNOPT is an efficient nonlinear equation solver that ignores any direct performance index and allows a different number of constraints and unknowns. For details see p. 78 the of SNOPT manual.[†]

1. Input seed for random number generator
2. Supply subroutines to calculate the initial and target orbits $\mathbf{r}^*_0(\tau_0)$, $\mathbf{v}^*_0(\tau_0)$ and $\mathbf{r}^*_f(\tau_f)$, $\mathbf{v}^*_f(\tau_f)$
3. Input upper and lower bounds for each of the global search parameters:
   α, β, S, $d\alpha/dt$, $d\beta/dt$, dS/dt, and problem specific parameters such as t_0, τ_0, τ_f if needed

DO WHILE ($propagations < propagations_{max}$)
   a. $propagations = propagations + 1$
   b. Populate global search parameters with random numbers
   c. Evaluate initial spacecraft position and velocity, $\mathbf{r}^*_0(\tau_0)$, $\mathbf{v}^*_0(\tau_0)$
   d. Fix initial spacecraft mass and mass co-state to a normalized 1 and -1 respectively
   e. Apply adjoint control transformation to obtain $\boldsymbol{\lambda}_{r0}$ and $\boldsymbol{\lambda}_{v0}$
   f. Propagate spacecraft state and co-state according to the implicit "bang-bang" structure
      At each successful integration step:
      1) Check for impact or escape. IF true THEN exit propagation
      2) Calculate the *norm* of constraints $\mathbf{r}_f - \mathbf{r}^*_f(\tau_f)$, $\mathbf{v}_f - \mathbf{v}^*_f(\tau_f)$
         For the planar DRO problem, it is sufficient to consider $\tau_f = \text{atan2}(r_2, r_1)$
      3) Store the associated flight time ($t_f = t$), and τ_f for a potential local search initial guess
      4) IF $norm_{min} < tolerance$ THEN
         a) Exit propagation
         b) Call local targeting routine with:
            Unknowns: $\boldsymbol{\lambda}_0$ and problem specific parameters such as t_0, τ_0, t_f, τ_f
            Constraints: $\mathbf{r}_f - \mathbf{r}^*_f(\tau_f)$, $\mathbf{v}_f - \mathbf{v}^*_f(\tau_f)$
         c) IF Converged THEN **record final unknown vector and associated properties**
      ELSE
         IF $t >= t_{max}$ THEN exit propagation
      ENDIF
END DO
4. Combine results with those from other processors (if any)
5. Compare each solution against all other solutions to identify the Pareto optimal set.

Fig. 4 Global low-thrust trade study algorithm.

Table 1 RTBP and propulsion parameters. All values are converted to LUs and TUs for implementation

Parameter	Value	Units
Jupiter–Europa distance	670,987.786940812	km
Jupiter Gm	126,686,537.857796	km^3/s^2
Europa Gm	3200.99980672059	km^3/s^2
Europa radius	1560.0	km
Earth–moon distance	384,400.0	km
Earth Gm	398,600.4415	km^3/s^2
Moon Gm	4902.801076	km^3/s^2
Moon radius	1738.0	km
Mass unit (m_0)	25,000.0	kg
T/m_0	0.199374249380613	mm/s^2
I_{sp}	7365.0	s
$g0$	9.80665	m/s^2

Table 2 Inputs for examples

Parameter	Europa DRO	Earth–moon
α_0, rad	$\pi + [-0.05, 0.05]$	$[-0.05, 0.05]$
$\dot{\alpha}_0$, rad/TU	$[-0.05, 0.05]$	$[-0.5, 0.5]$
S_0, natural units[a]	$[0.01, 0.21]$	$\lambda_{m0} m_0/c + [0, 0.03]$
$\dot{S}_0$, natural units	$[-0.002, 0]$	$[-0.01, 0]$
Max flight time during global search, days	125	125
Global search constraint tolerance for transferring to local search	5%	40%
Local search convergence tolerance	0.00001%	0.00001%

[a]From Eq. (23), S must be greater than $\lambda_m m_0/c$ in order for λ_v to be positive. For DRO and moon examples, respectively, $\lambda_{m0} m_0/c = -0.1902, -0.014185$ (natural units).

Global Search Strategy

The global search space primarily consists of the adjoint control variables $(\alpha_0, \dot{\alpha}_0, \beta_0, \dot{\beta}_0, S_0, \dot{S}_0)$. If the specific problem is free initial time, free initial orbit phase, and/or free final orbit phase, then t_0, τ_0, and τ_f are included, respectively. However, because we check the constraint violations at every successful step of the orbit propagation, t_f is not a required global guess variable. Additionally, if the final orbit is a simple closed orbit and τ_f is some angle that is a function of the spacecraft state, then τ_f can be calculated at every step of the orbit propagation and also removed from the global search list. Of course bounds must be input for each of the global search variables. The global search space is populated with uniformly distributed random numbers.

For each set of randomly generated unknowns, one propagation of Eq. (24) is required, noting that during the global search mode, the additional 14^2 equations associated with the state transition matrix do *not* need to be propagated. The final constraint conditions are checked at each successful time step during the integration. If the final conditions are met at any time step to a prespecified tolerance, then the global search mode is suspended, and the current subproblem is fed into a full gradient-based targeting routine that attempts to adjust the unknown vector to drive the constraint conditions to zero. The state transition matrix of course is propagated along with the state during the local search mode. If the problem

[†]Data available online at http://www.sbsi-sol-optimize.com/manuals/SNOPT%20Manual.pdf [cited 28 May 2006].

Table 3 Results and statistics for examples

Parameter	Europa DRO	Earth–moon
Number of global propagations	1,808,909	29,451,163
Number of local attempts	106,494	275,602
Number of local converged	51,032	21,372
Number of Pareto optimal	3208	47
Number of processors (Pentium 4 Xeon 3.2 GHz)	200	400
Run time per processor, min	60	240
Total processor run time, min	12,000	96,000
Average number of local solutions attempted per minute per processor	8.87	2.87
Average number of converged solutions per minute per processor	4.25	0.223
Ratio of non-Pareto optimal to Pareto optimal	15.91	454.7

converges, the time, Δv, the unknown vector, and other pertinent characteristics of the solution are recorded. Regardless of convergence, if the number of global propagations is less than a user specified maximum, then the algorithm is shifted back to the global search mode and the process is repeated. In this manner, the algorithm will ideally accumulate a large sample of solutions that span a wide range of feasible flight times and Δv. The nature of the uniformly random global search is ideal for parallel applications because the speedup for additional processors is exactly linear. Once the solutions are assembled into one large set, the flight time and Δv values for each solution are compared against all other solutions to identify the Pareto front. Again, as Fig. 3 illustrates, a Pareto optimal solution finds no other solution that is superior in both flight time and Δv [40].

Figure 4 presents an overview of the global search algorithm. Tuning the algorithm consists primarily of adjusting the boundaries on the unknown global search variables. Although the local search is initiated with the bounded guesses from the global search, once the

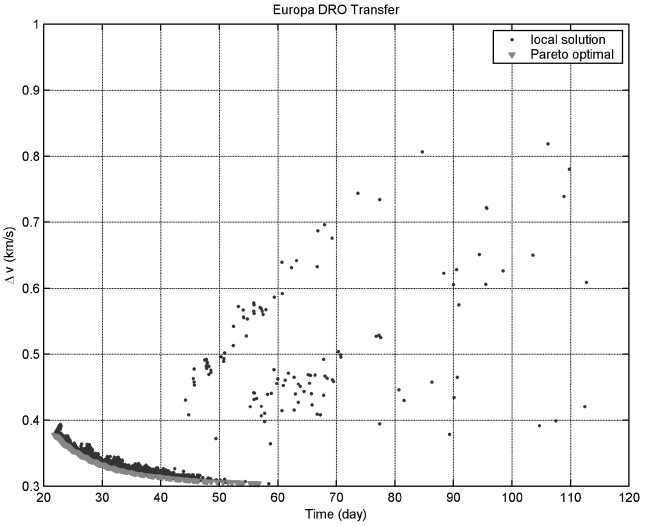

Fig. 5 Results from the Europa DRO transfer example. In total there are 51,032 converged solutions including 3208 that are Pareto optimal.

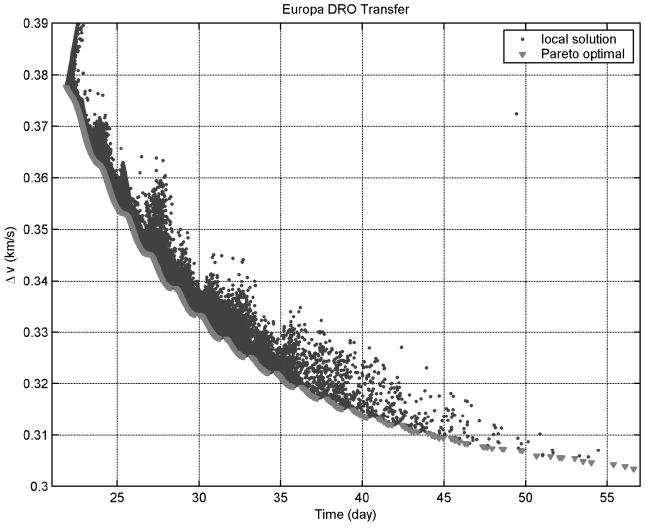

Fig. 6 Zoomed view of Fig. 5.

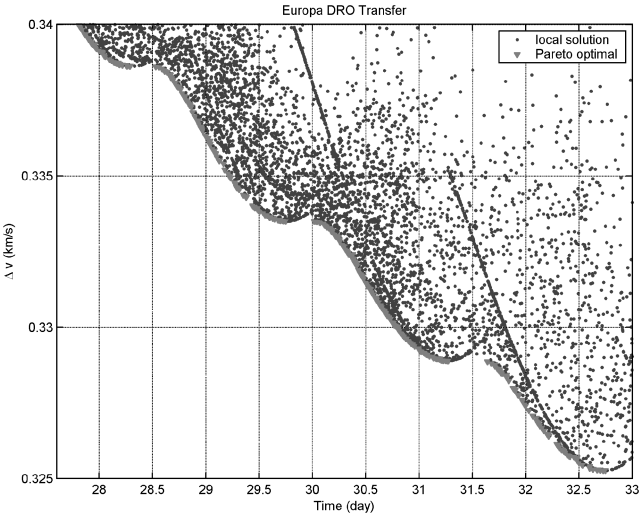

Fig. 7 Zoomed view of Fig. 6.

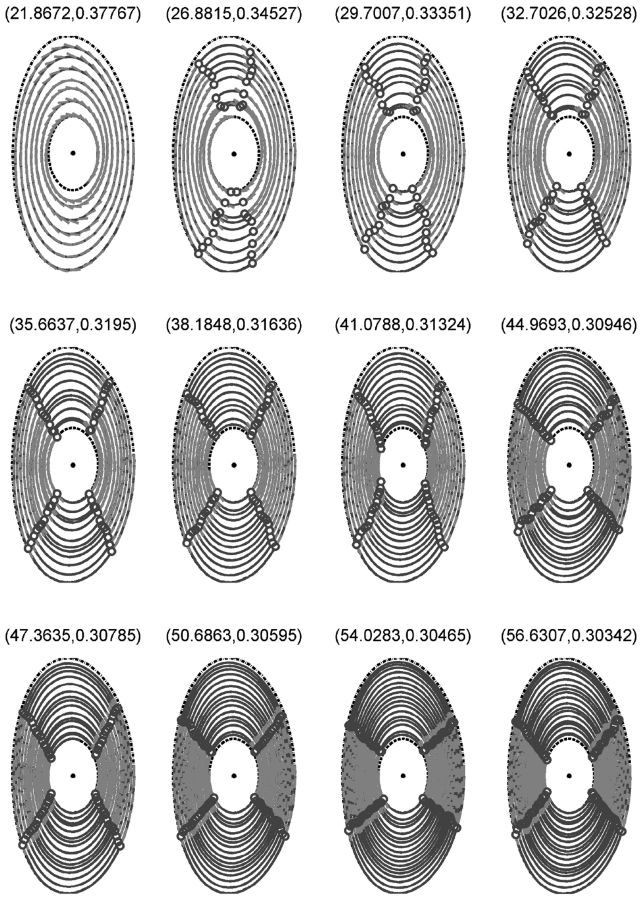

Fig. 8 Representative Pareto optimal trajectories from the Europa DRO example. The subtitles are labeled (TOF, Δv) in days and km/s.

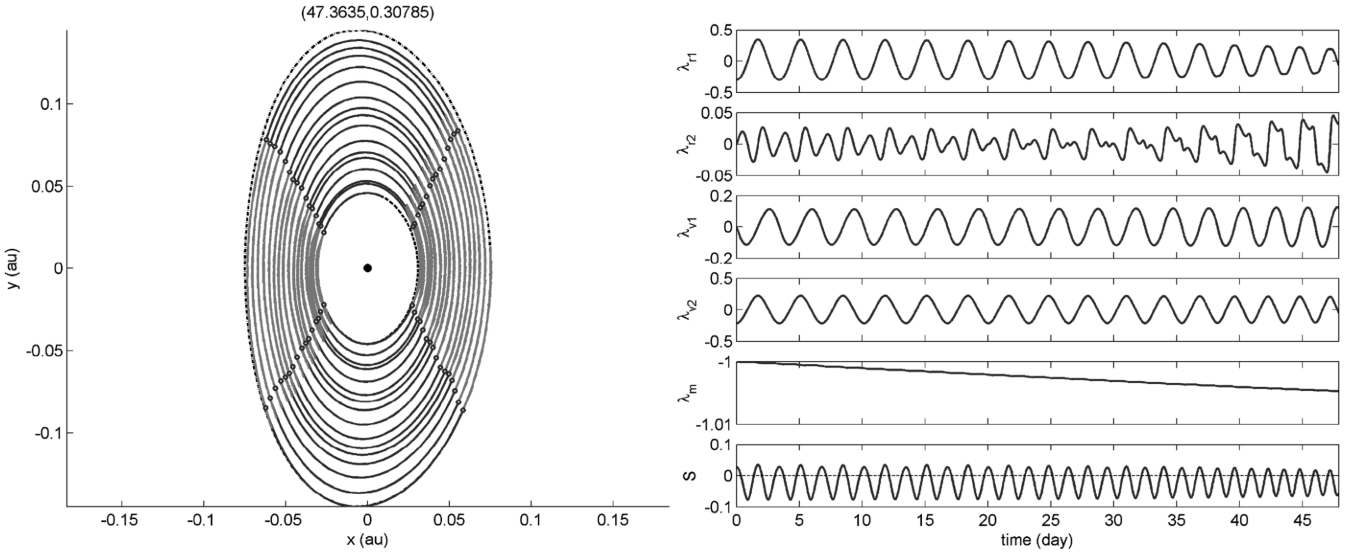

Fig. 9 Example Pareto optimal trajectory and evolution of the costates and switching function.

algorithm transitions to the local mode, it is free to move in any direction the gradients suggest.

Examples and Results

In this section, the algorithm is tested on two multiple-revolution problems in the RTBP. Table 1 gives values for the required numerical parameters. The propulsion inputs and initial mass are common for each example. The algorithm is run in parallel on the Jet Propulsion Laboratory's Cosmos Cluster. The accuracy of the orbit propagation is such that the Jacobi constant C generally remains constant to 15 significant digits over a coast leg, and the switching times are interpolated such that $S = 0$ to at least 13 digits. As a separate check, H is found to be constant to at least 11 significant digits over the entirety of a given trajectory.

In both examples, we solve an orbit transfer with the initial time and phase fixed and the final time and phase free. Both problems are constrained to the planar case for simplicity. The unknown vectors for the global and local searches are given, respectively, in Eq. (31) while the constraint vector for both searches is Eq. (32). As discussed earlier, the transversality conditions are implicitly targeted via the Pareto front in lieu of including them explicitly in Eq. (32). The initial mass and mass costate are set to a normalized value of 1 and −1, respectively. Both examples involve targeting DROs in restricted three body problems. The orbits are numerically parameterized with a polar angle τ as described in [41]. This functional approximation is required to evaluate the constraint vector in Eq. (32) and its derivative with respect to τ.

$$\text{global search} \Rightarrow \boldsymbol{U}_{4\times1}^{\mathsf{T}} = (\alpha\ \dot{\alpha}\ S\ \dot{S}), \quad (t_f, \tau_f) \text{ solved implicitly}$$
$$\text{local search} \Rightarrow \boldsymbol{U}_{6\times1}^{\mathsf{T}} = (\boldsymbol{\lambda}_{r0}^{\mathsf{T}}\ \boldsymbol{\lambda}_{v0}^{\mathsf{T}}\ \tau_f\ t_f) \tag{31}$$

$$\boldsymbol{C}_{4\times1}^{\mathsf{T}} = [\boldsymbol{r}_f^{\mathsf{T}} - \boldsymbol{r}^{*\mathsf{T}}(\tau_f)\ \ \boldsymbol{v}_f^{\mathsf{T}} - \boldsymbol{v}^{*\mathsf{T}}(\tau_f)] \tag{32}$$

Europa DRO Transfer Example

The first example is a planar transfer from a large DRO to a smaller DRO at Europa. Distant retrograde orbits are a simple family of periodic orbits in the RTBP that evolve from planar retrograde circular orbits near Europa into near-ellipse shaped orbits with Europa at the center. See, for example, [32,41]. The initial conditions are

$$r_1 = 0.07517684416232644 \text{ LU}$$

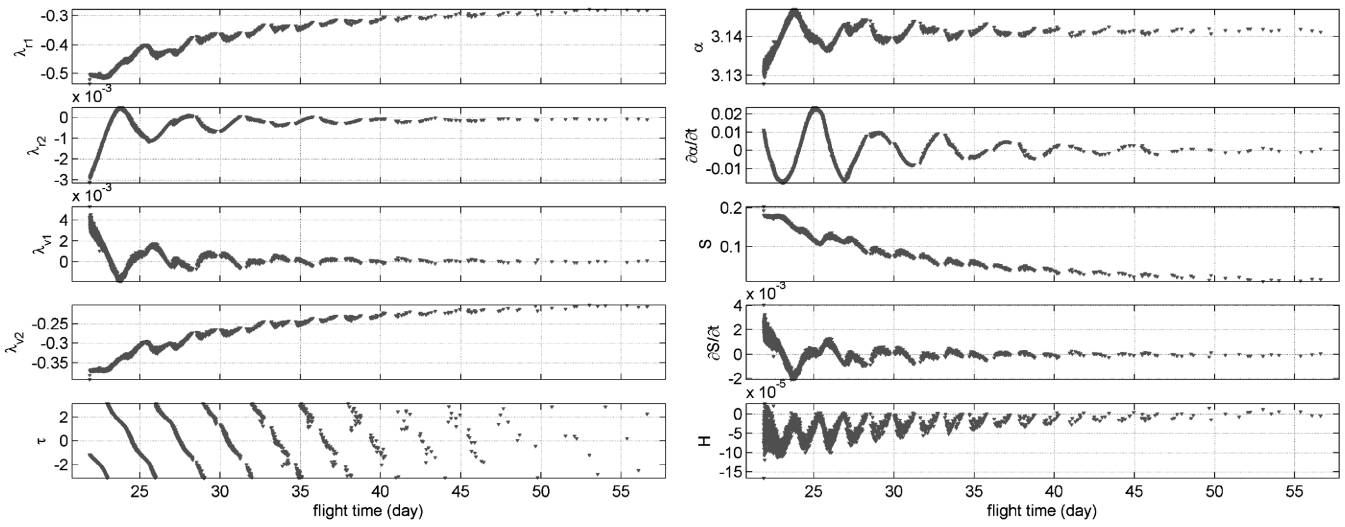

Fig. 10 Characteristics of all Pareto optimal trajectories from the Europa DRO example. Left: converged unknown vector (initial costates, target orbit phase, and flight time). Right: calculated values (initial adjoint control variables and Hamiltonian). All values are expressed in natural units.

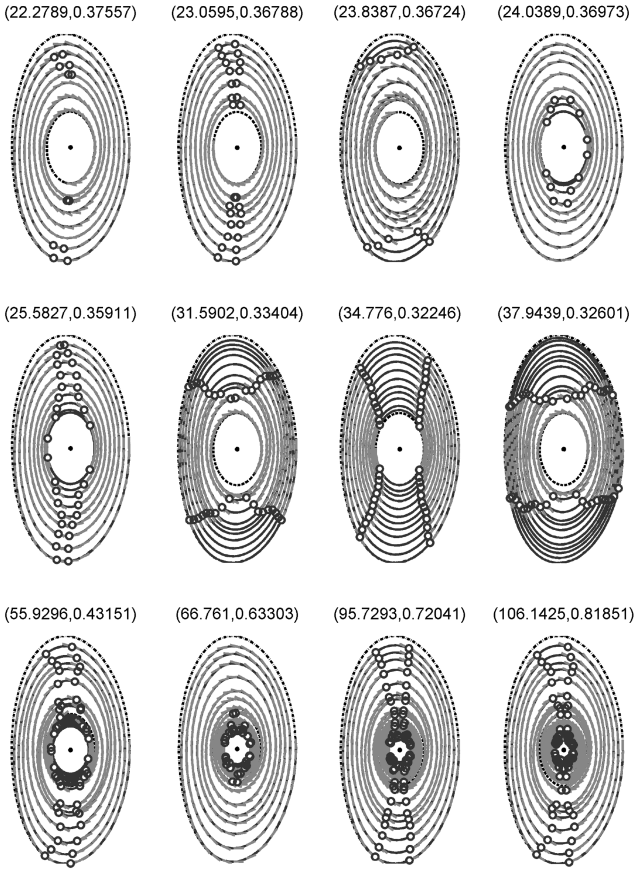

Fig. 11 Representative non-Pareto optimal solutions. Europa DRO transfer. Note the final row demonstrates pathological cases that spiral well past (but eventually return to) the target orbit.

$$v_2 = -0.149921522008374 \text{ LU/TU}$$

$r_2 = v_1 = 0$, while the target orbit is phase free with an r_1 axis crossing of 0.0306707376649 LU. The second columns of Tables 2 and 3 summarize the inputs and results, respectively. The algorithm is tested first with large bounds on the initial control variables, and ranges are then successively adjusted to cover the region where most of the solutions are clustered. The final ranges used in this example (and the following example) are by no means optimal; in general, solutions exist for a wide range of bounds and those reported are found to be sufficient.

Nearly 2×10^6 global search propagations produced 51,032 converged solutions, where 3208 are Pareto optimal. Figures 5–7 show three different views of the resulting converged trajectories plotted on the plane of the competing objectives: flight time and Δv. Each point on the figures represents a converged trajectory that satisfies the necessary conditions for mass optimality associated with the specific converged value of flight time and final target orbit phase. The Pareto optimal solutions are labeled as downward pointing triangles and the Pareto front is the set of discrete Pareto optimal solutions. Note, the reported flight times do not include coasts (if present) at the beginning or end of the converged trajectories. The wave structure of the Pareto front is related to the number of spacecraft revolutions. Although there is no formal evidence of global optimality, the smoothness and fullness of the Pareto front gives confidence that its solutions are indeed associated with global minima.

Example Pareto optimal trajectories are shown in Figs. 8 and 9. The initial and final orbits are shown as the outer and inner dashed lines, respectively. The circles on the trajectory plots illustrate the switching times. Lighter colored lines are the thrusting directions and are generally aligned opposite to the velocity. Although the exact directions may be difficult to discern from the figures, the bang-bang structure of the thrusting is clearly illustrated and leads to solutions that cycle the thrust on and off twice per revolution. As an example, the solution in Fig. 9 includes 16 revolutions and 63 switching times. Note, the solutions maintain similar thrusting profiles across the full range of flight times. This optimal thrusting structure associated with the DRO to DRO transfer is an important result that is relevant to the trajectory design of future low-thrust missions to planetary moons.

Figure 10 plots the initial control variables and associated initial costates, the final orbit phase, and the Hamiltonian against the time of flight for each of the Pareto optimal solutions. Notice the optimal final orbit phase is almost linearly related to flight time for much of the range. The continuity of all the variables further indicates that all of the Pareto optimal solutions are members of the same family of solutions. The initial switching functions in this problem are all positive as the bounds on the global search variables in Table 2 suggest. As expected, the optimal initial thrust angle α_0 departs only slightly from π, the antivelocity direction. For some applications, it may be useful to curve fit data from Fig. 10 to approximate the family of Pareto optimal solutions [16].

Note from the discussion at the bottom of the TPBVP section, one of the transversality conditions for the time-free orbit transfer requires the final Hamiltonian to be zero. Figure 10 shows that the Hamiltonian values for the Pareto optimal solutions cycle roughly through zero every 1.5 days. As the transversality condition predicts, this zero crossing coincides exactly with the local extrema across the flight time seen on the Pareto front. For example, from Fig. 10, H is near zero and from Fig. 7, minima exist on the Pareto front at flight times of $\{28.25, 29.75, 31.25, 32.75\}$ days. Thus both the Pareto front and the transversality condition lead to the same optimal flight times. The Pareto front, however, has the significant advantage of distinguishing a minimum from a maximum or a stationary point, whereas the transversality condition $H = 0$ is only a necessary condition for an extremal with respect to the final time. Looking at Fig. 10, H appears to quickly pass through zero twice at the top of each cycle. This first crossing likely corresponds to the minimum on the Pareto front whereas the second crossing corresponds to the neighboring maximum almost immediately to the right. To verify, we would need to target the $H = 0$ condition explicitly.

Figure 11 shows a sampling of the solutions that are *not* Pareto optimal. However, it is emphasized that each trajectory does indeed meet the necessary conditions for optimality for the time-fixed, phase-fixed subproblem. The trajectories on the first two rows generally have different thrusting structures, but suffer relatively small hits in performance compared to the Pareto optimal solutions. The last row, however, is composed of the pathological cases that suffer tremendously in flight time and Δv because the trajectories spiral past the target orbit yet manage to eventually spiral back to the exact target conditions. In the case of the last orbit in the third row, the trajectory spirals down to a near-circular orbit around 7900 km,

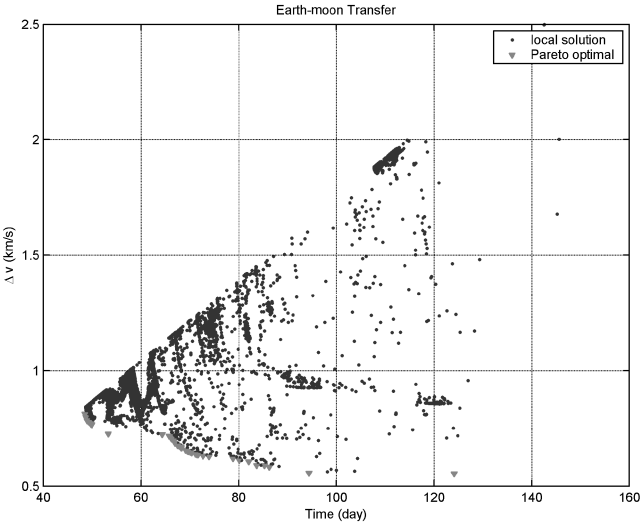

Fig. 12 Results from the Earth–moon transfer example.

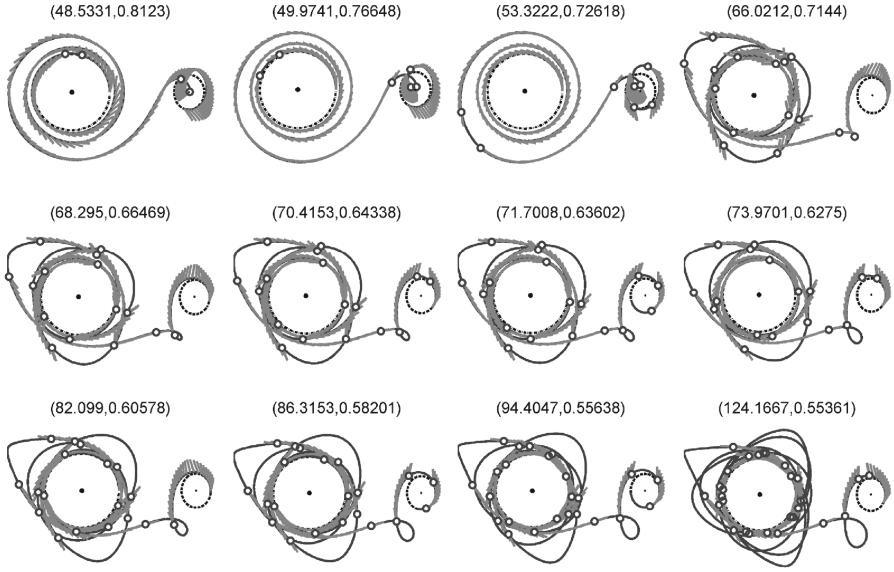

Fig. 13 Representative Pareto optimal trajectories for the Earth to moon transfer example.

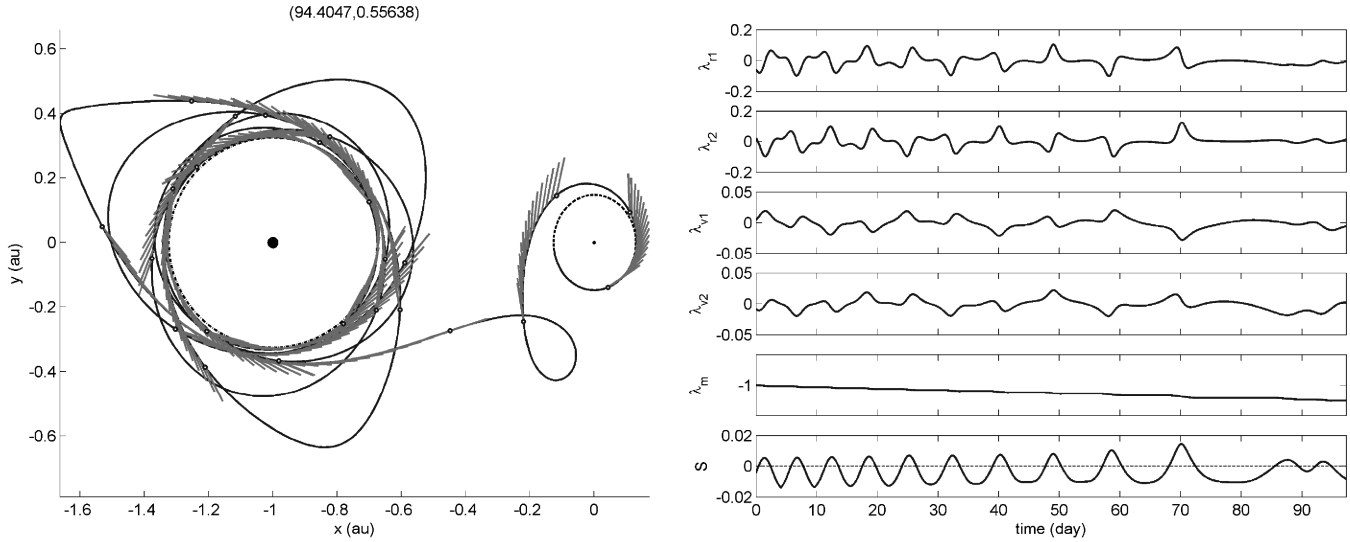

Fig. 14 Example Pareto optimal trajectory and evolution of the costates and switching function.

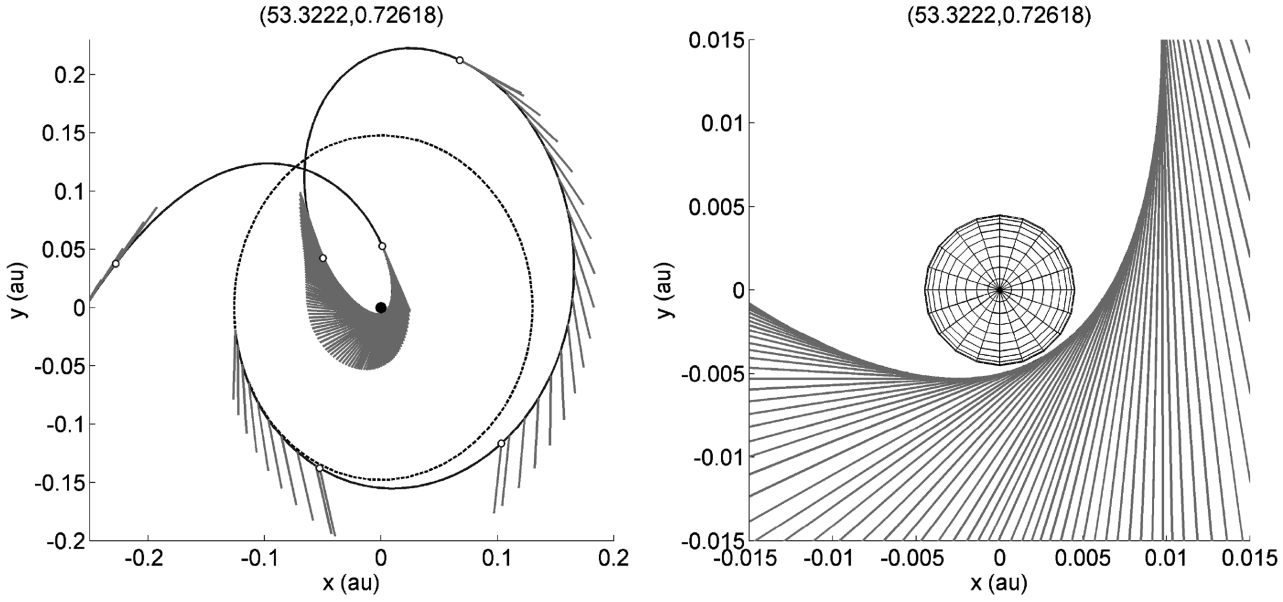

Fig. 15 Grazing moon flyby on the example Pareto optimal solution. Right: Zoomed view.

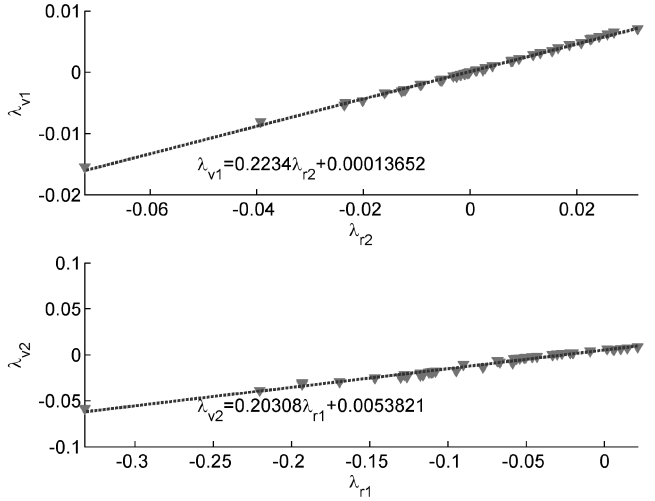

Fig. 16 Empirical near-linear relationships between initial Pareto optimal costates.

coasts for about 50 days, then spirals back to the 20,000 km target DRO with a total of 80 switching times, 97 revolutions, and a 106 day flight time. Although this solution is not useful from a mission design perspective, it highlights the capabilities of the local targeting method. Remarkably, despite the sensitivity associated with nearly 100 revolutions and switching times, the local search routine successfully drives this solution to convergence with less that 0.00001% error. Generally, a multiple shooting method [18,19,42] or some type of guidance control law [43,44] is required to target or optimize a trajectory with so many revolutions.

Earth to Moon Transfer Example

The second example is a planar transfer from a direct near-circular 125,000 km orbit at Earth to a 50,000 km DRO at the moon. The initial conditions are $r_1 = -0.674817898022893$ LU, $v_2 = 1.41785636974331$ LU/TU, $r_2 = v_1 = 0$. The target orbit is phase free with an r_1 axis crossing of 0.130072840790843 LU. The third columns of Tables 2 and 3 summarize the inputs and results, respectively.

The dynamics associated with this second example are more complicated because the trajectories circulate both primaries. Accordingly, the algorithm finds converged solutions roughly an order of magnitude less frequently than in the Europa example. For the Earth–moon transfer, almost 30×10^6 global search propagations resulted in 21,372 converged solutions, where 47 are Pareto optimal. The complicated orbit transfer leads to a variety of family types. As a result, the solutions populate a much larger region of the flight time-Δv plane than we saw in the previous example. Based on this scattering, this problem would likely benefit from a global search technique that drives solutions toward the Pareto front, such as the evolutionary techniques employed in [29,30]. Looking at Fig. 12, it is immediately apparent that the solutions are bounded on the top by the line that passes through (0,0). A similar ceiling is seen in the Europa example on the far left side of Fig. 6. This linear relationship between thrust and flight time is of course a result of the continuous thrusting case.

The diversity of the solutions leads to a disjointed Pareto front as seen in Fig. 12. For example, the Pareto solutions disappear in the vicinity of 60 day flight times because the family of solutions on the left, in particular the one outstanding member at (53.3, 0.726), dominates all of the nearby solutions that likely are in different families. Figures 13 and 14 give a sampling of the Pareto optimal trajectories, and as suspected the solutions towards the left represent an isolated family that includes a close flyby of the moon. In general, the trajectories complete from 3–10 Earth revolutions followed by either a distant or close moon flyby before the DRO insertion.

Figure 15 presents a closer view of the third trajectory on the first row of Fig. 13. It reveals a powered flyby that closely avoids impact (and consequently a failed exit from the local search). Its Pareto optimality status hints that the performance will improve if this minimum altitude constraint is relaxed. Upon close inspection, all 15 Pareto optimal solutions with flight times less than 60 days include similar grazing flybys, while the non-Pareto solutions in the vicinity include similar flybys but at increasing altitudes. Similar to the rationale of implicitly solving the transversality conditions, the grazing flyby example demonstrates this method's ability to enforce nonlinear inequality constraints without including them explicitly in the TPBVP.

Figure 16 documents an observed near-linear relationship between pairs of the Pareto optimal initial costates. Although the origin of this relationship is unclear, it could prove useful for finding neighboring solutions. Figure 17 shows the converged values for the initial costates and associated initial control variables, the final orbit phase, and the Hamiltonian against the time of flight for each of the Pareto optimal solutions.

Figure 18 illustrates the converged trajectories for several of the interesting non-Pareto optimal solutions. Regardless of performance, it should be reemphasized that each converged solution does in fact meet the necessary optimality conditions for the phase-fixed time-fixed subproblem. Although some of the solutions appear to take the same shape as their Pareto optimal counterparts, others, particularly those with the longer flight times, take very different paths. Note, many of the solutions naturally approach the stable

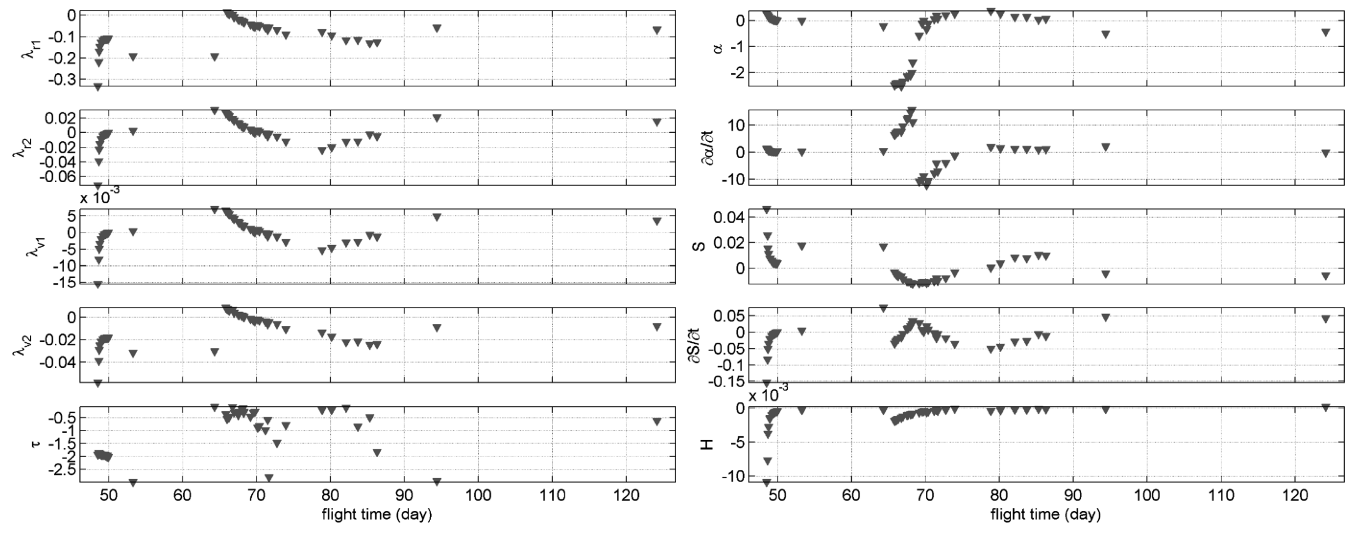

Fig. 17 Pareto front characteristics of the Earth–moon example. See Fig. 10 caption.

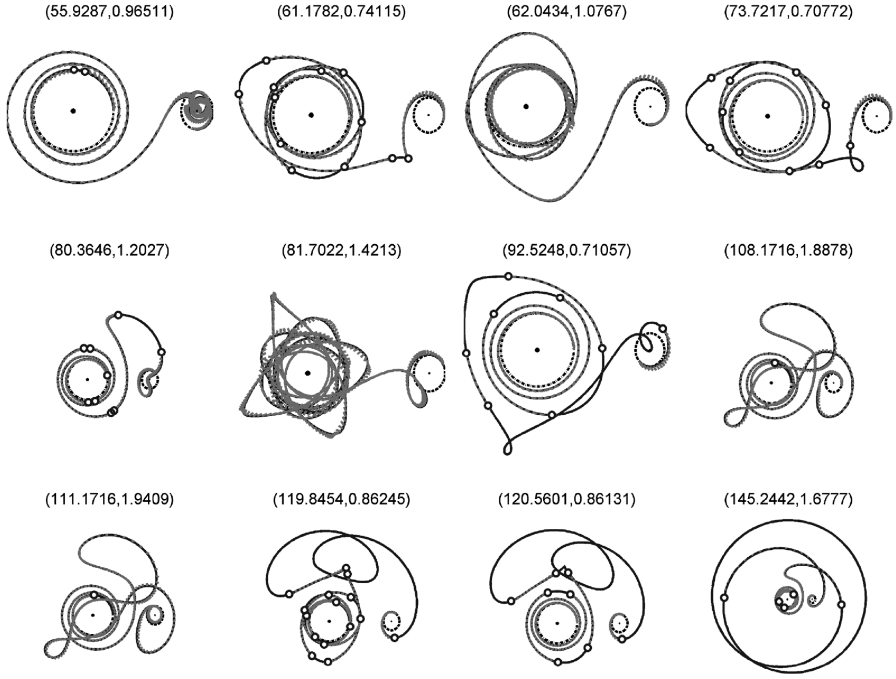

Fig. 18 Representative non-Pareto optimal solutions for the Earth to moon example.

manifolds associated with the unstable families of periodic orbits about the moon.

Conclusions

A global low-thrust trade study tool is developed in a general form and applied specifically to multiple revolution orbit transfers in the restricted three body model. The sensitivity problems generally associated with indirect shooting methods are combated with analytic derivatives and an expansive global search that initiates a local search only when a guess is deemed in the vicinity of a solution. An implicit bang-bang orbit propagator is described complete with the equations to map its derivatives across the switching times. As a result, complicated multiple-revolution, multiple-thrust-arc trajectories are parameterized using just a few initial control variables and no patch points. Although the initial setup is admittedly tedious, the derived equations for the Jacobian and analytic derivatives are valid for an important class of low-thrust optimal control problems. Further, as demonstrated by the Pareto optimal solutions that find grazing flybys of the moon, the method easily allows the inclusion of nonlinear inequality constraints without modification of the setup by simply discarding any trajectories that violate the constraint.

The low dimensionality is well suited for a global search for the local gradient-based solutions. The nature of a global search and the built-in potential for coasting leads naturally to solutions across a full range of flight times. The multiobjective search is a powerful tool for mission design where the classic dilemma is to choose between flight time and fuel.

The Pareto optimal solutions are found in a single parallel run and may consist of one continuous family or a diverse set of isolated families or solutions. The Pareto optimality concept is particularly useful in problems that include many locally optimal solutions as is the case for the general low-thrust problem. Although there is no guarantee that a Pareto optimal solution is globally optimal for the original problem, it does, however, represent a global optimum among the set of local solutions.

The parallel speedup is exactly linear and is demonstrated by implementing the algorithm on several hundred nodes. Although this many processors may be unavailable to most researchers, in both example cases this proof of concept led to tens of thousands of converged solutions, clearly more than enough to sample the search space. For example, if a researcher is limited to one processor running for 1 day, he or she could expect to find over 6000 and 300 converged solutions, respectively, to the first and second example problems. Although this approach fails to appreciate the advantages of the linear parallel speedup, it nonetheless sheds significant insight into the multiobjective solution space.

The algorithm can be slightly modified to include different constraints or even alternative search strategies such as explicitly targeting any transversality conditions or directly minimizing Δv. In any case, the benefits of sampling a low dimensioned search space remain, and the results can lead to a global perspective of optimal trajectories across the competing objectives of flight time and Δv.

Acknowledgements

Part of this work was carried out at the Jet Propulsion Laboratory, California Institute of Technology, under a contract with the National Aeronautics and Space Administration. The author is grateful to Anastassios Petropoulos, Seungwon Lee, Richard Terrile, Paul von Allmen, Wolgang Fink, and Jon Sims for contributing support and discussions.

References

[1] Lawden, D. F., *Optimal Trajectories for Space Navigation*, Butterworths, London, 1963, pp. 5, 59.
[2] Marec, J.-P., *Optimal Space Trajectories*, Elsevier, Amsterdam, 1979, p. 54.
[3] Jezewski, D. J., "Primer Vector Theory and Applications," NASA TR R-454, Lyndon B. Johnson Space Center, Houston, TX, Nov. 1975.
[4] Melbourne, W. G., and Sauer, C. G., Jr., "Optimum Interplanetary Rendezvous Trajectories with Power Limited Vehicles," *AIAA Journal*, Vol. 1, Jan. 1963, pp. 54–60.
[5] Sauer, C. G., Jr., "Optimization of Multiple Target Electric Propulsion Trajectories," AIAA Paper 73-205, Jan. 1973.
[6] Bryson, A. E., and Ho, Y. C., *Applied Optimal Control*, Blaisdell, Waltham, MA, 1969, Chaps. 2, 3.
[7] Hull, D. G., *Optimal Control Theory for Applications*, Springer, New York, 2003, p. 167, Chaps. 6–17.
[8] Prussing, J. E., "Illustration of the Primer Vector in Time- Fixed, Orbit Transfer," *AIAA Journal*, Vol. 7, No. 6, 1969, pp. 1167–1168.
[9] Prussing, J. E., and Chiu, J. H., "Optimal Multiple-Impulse Time-Fixed Rendezvous Between Circular Orbits," *Journal of Guidance, Control, and Dynamics*, Vol. 9, No. 1, 1986, pp. 17–22.
[10] Sauer, C. G., Jr., "MIDAS—Mission Design and Analysis Software for the Optimization of Ballistic Interplanetary Trajectories," *Journal of the Astronautical Sciences*, Vol. 37, July–Sept. 1989, pp. 251–259.
[11] Lion, P. M., and Handelsman, M., "Primer Vector on Fixed-Time

Impulsive Trajectories," *AIAA Journal*, Vol. 6, No. 1, 1968, pp. 127–132.
[12] Jezewski, D. J., and Rozendaal, H. L., "An Efficient Method for Calculating Optimal Free-Space N-Impulse Trajectories," *AIAA Journal*, Vol. 9, No. 4, 1971, pp. 760–763.
[13] Guzman, J. J., Mailhe, L. M., Schiff, C., Hughes, S. P., and Folta, D. C., "Primer Vector Optimization: Survey of Theory, New Analysis and Applications," IAC Paper 020A.6.09, 2002.
[14] Senet, J., and Ocampo, C., "Low-Thrust Variable Specific Impulse Transfers and Guidance to Unstable Periodic Orbits," *Journal of Guidance, Control, and Dynamics*, Vol. 28, No. 2, 2005, pp. 280–290.
[15] Ranieri, C. L., and Ocampo, C. A., "Optimization of Round-Trip, Time-Constrained, Finite-Burn Trajectories via and Indirect Method," *Journal of Guidance, Control, and Dynamics*, Vol. 28, No. 2, 2005, pp. 306–314.
[16] Ranieri, C. L., and Ocampo, C. A., "Indirect Optimization of Spiral Trajectories," AAS Paper 05-372, 2005.
[17] Zimmer, S., and Ocampo, C. A., "Analytical Gradients for Gravity Assist Trajectories Using Constant Specific Impulse Engines," *Journal of Guidance, Control, and Dynamics*, Vol. 28, No. 4, 2005, pp. 753–760.
[18] Nah, R. S., Vadali, S. R., and Braden, E., "Fuel-Optimal, Low-Thrust, Three-Dimensional Earth–Mars Trajectories," *Journal of Guidance, Control, and Dynamics*, Vol. 24, No. 6, 2001, pp. 1100–1107.
[19] Vadali, S. R., Nah, R., Braden, E., and Johnson, I. L., Jr., "Fuel-Optimal Planar Earth–Mars Trajectories Using Low-Thrust Exhaust-Modulated Propulsion," *Journal of Guidance, Control, and Dynamics*, Vol. 23, No. 3, 2000, pp. 476–482.
[20] Kluever, C. A., and Pierson, B. L. "Optimal Low-Thrust Three-Dimensional Earth-Moon Trajectories," *Journal of Guidance, Control, and Dynamics*, Vol. 18, No. 4, 1995, pp. 830–837.
[21] Moore, G., E., "Cramming More Components onto Integrated Circuits," *Electronics*, Vol. 38, No. 8, 1965, pp. 114–117.
[22] Enright, P. J., and Conway, B. A., "Optimal Finite-Thrust Spacecraft Trajectories Using Collocation and Nonlinear Programming," *Journal of Guidance, Control, and Dynamics*, Vol. 14, No. 5, 1991, pp. 981–985.
[23] Fahroo, F., and Ross, I. M., "Direct Trajectory Optimization by a Chebyshev Pseudospectral Method," *Journal of Guidance, Control, and Dynamics*, Vol. 25, No. 1, 2002, pp. 160–166.
[24] Hargraves, C. R., and Paris, S. W., "Direct Trajectory Optimization Using Nonlinear Programming and Collocation," *Journal of Guidance, Control, and Dynamics*, Vol. 10, No. 4, 1987, pp. 338–342.
[25] Bellman, R. E., and Kalaba, R., *Dynamic Programming and Modern Control Theory*, Academic Press, New York, 1965, Chap. 3.
[26] Whiffen, G. J., and Sims, J. A., "Application of the SDC Optimal Control Algorithm to Low-Thrust Escape and Capture Trajectory Optimization," AAS Paper 02-208, 2002.
[27] Gill, P. E., Murray, W., and Saunders, M. A., "SNOPT: An SQP Algorithm For Large Scale Constrained Optimization," *SIAM Journal of Optimization*, Vol. 12, No. 4, 2002, pp. 979–1006.
[28] Russell, R. P., and Ocampo, C. A., "Global Search for Idealized Free-Return Earth–Mars Cyclers," *Journal of Guidance, Control, and Dynamics*, Vol. 28, No. 2, 2005, pp. 194–208.
[29] Lee, S., Russell, R. P., Fink, W., Terrile, R. J., Petropoulos, A. E., and von Allmen, P., "Low-Thrust Mission Trade Studies with Parallel, Evolutionary Computing," *IEEE Aerospace Conference*, IEEE Publications, Piscataway, NJ, 2006.
[30] Lee, S., and Russell, R. P., "Multi-Objective Parallel Genetic Algorithms Applied to the Primer Vector Control Law," AAS Paper 06-196, 2006.
[31] Mulder, F. A., "Optimal Finite Burn Transfer Trajectories Using an Indirect Method with Suboptimal Starting Iterates," M.S. Thesis, University of Texas at Austin, May 2004.
[32] Ocampo, C. A., "Trajectory Optimization for Distant Earth Satellites and Satellite Constellations," Ph.D. Thesis, Department of Aerospace Engineering, University of Colorado, Oct. 1996. pp. 18, 53.
[33] Prussing, J. E., and Suzannah, L. S., "Second-Order Necessary Conditions and Sufficient Conditions Applied to Continuous-Thrust Trajectories," *Journal of Guidance, Control, and Dynamics*, Vol. 28, No. 4, 2005, pp. 812–816.
[34] Thorne, J. D., and Hall, C. D., "Approximate Initial Lagrange Costates for Continuous-Thrust Spacecraft," *Journal of Guidance, Control, and Dynamics*, Vol. 19, No. 2, 1996, pp. 283–288.
[35] Dixon, L. C. W., and Biggs, M. C., "The Advantages of Adjoint-Control Transformations when Determining Optimal Trajectories by Pontryagin's Maximum Principle," *Aeronautical Journal*, Vol. 76, No. 735, 1972, pp. 169–174.
[36] Yan, H., and Wu, H., "Initial Adjoint-Variable Guess Technique and Its Application in Optimal Orbital Transfer," *Journal of Guidance, Control, and Dynamics*, Vol. 22, No. 3, 1999, pp. 490–492.
[37] Hull, D. G., "Numerical Derivatives for Parameter Optimization," *Journal of Guidance, Control, and Dynamics*, Vol. 2, No. 2, 1979, pp. 158–160.
[38] Griffith, D. T., Turner, J. D., Vadali, R. S., and Junkins, J. L., "Higher Order Sensitivities for Solving Nonlinear Two-Point Boundary-Value Problems," AIAA 2004-5404, 2004.
[39] Battin, R. H., *An Introduction to the Mathematics and Methods of Astrodynamics*, AIAA, New York, 1987, p. 453.
[40] Collete, Y., and Siarry, P., *Multi-Objective Optimization, Principles and Case Studies*, Springer–Verlag, Berlin, 2003, pp. 15–43.
[41] Hirani, A. N., and Russell, R. P., "Approximations of Distant Retrograde Orbits for Mission Design," AAS Paper 06-116, 2006.
[42] Gao, Y., and Kluever, C., "Low-Thrust Interplanetary Orbit Transfers Using Hybrid Trajectory Optimization Method with Multiple Shooting," AIAA 2004-5088, 2004.
[43] Petropoulos, A. E., "Low-Thrust Orbit Transfers Using Candidate Lyapunov Functions with a Mechanism for Coasting," AAS Paper 04-5089, 2004.
[44] Kluever, C. A., "Simple Guidance Scheme for Low-Thrust Orbit Transfers," *Journal of Guidance, Control, and Dynamics*, Vol. 21, No. 6, 1998, pp. 1015–1017.